ORIGINAL PAPER

Relationships between landscape morphology, climate and surface erosion in northern Peru at 5°S latitude

R. Mettier · F. Schlunegger · H. Schneider · D. Rieke-Zapp · M. Schwab

Abstract The northern segment of the Peruvian Andes is affected by a twofold climate with measurable implications on landscapes and landscape dynamics. During 'normal' or 'neutral' years easterly winds bring rain from the Atlantic and the Amazon Basin to the Sierras, which results in a seasonal climate with rather low-intensity precipitations. In contrast, during the large-scale warm phase of the ENSO cycle, El Niños transfer moisture from the Pacific to the Peruvian coast by westerly winds and result in high-intensity precipitation. We investigate the effects of this twofold climate for the case of the Piura drainage basin at ca. 5°S latitude (northern Peru). In the headwaters that have been under the influence of the easterlies, the landscape is mantled by a thick regolith cover and dissected by a network of debris flow channels that are mostly covered by a thick layer of unconsolidated sediment. This implies that in the headwaters of the Piura River sediment discharge has been limited by the transport capacity of the sediment transfer system. In the lower segment that has been affected by high-intensity rainfall in relation to the westerlies (El Niños), the hillslopes are dissected by debris flow channels that expose the bedrock on the channel floor, implying a supply-limited sediment discharge. Interestingly, measurements at the Piura gauging station near the coast reveal that, during the last decades, sediment was transferred to the lower reaches only in response to the 1982–1983 and 1997–1998 El Niño periods. For the latter period, synthetic aperture radar (SAR) intensity images show that the locations of substantial erosion are mainly located in areas that were affected by higher-than-average precipitation rates. Most important, these locations are coupled with the network of debris flow channels. This implies that the seasonal easterlies are responsible for the production of sediment through weathering in the headwaters, and the highly episodic El Niños result in export of sediment through channelized sediment transport down to the coastal segment. Both systems overlap showing a partially coupled sediment production–delivery system.

Keywords Geomorphology · Precipitation and erosion · Northern Peru · SAR and change detection

Introduction

It has been recognized that climate imprints the mountain landscape and plays an important role in scaling sediment production by weathering, and the sediment transfer by fluvial and associated hillslope processes (e.g., Kirchner et al. 2001, 2003; Reiners et al. 2003; Kober et al. 2007). The Piura drainage basin that is located at the western escarpment of the Peruvian Andes at 5°S latitude (Fig. 1) is an ideal region for exploring potential relationships between climate and the landscape's morphology. This is the case because this region (Fig. 1b) experiences an easterly-wind-driven monsoonal climate in the Sierras, and episodic westerly-wind-driven precipitation, associated with El Niños, at the Pacific coast. Recently, higher-than-average precipitation rates were measured at the Pacific coast during the 1983–1984 and 1997–1998 El Niño events. In this paper, we reconstruct the landscape's response to climate for the situation of the Piura drainage basin (Fig. 1b) by two approaches. In a first step, we

R. Mettier · F. Schlunegger (✉) · H. Schneider ·
D. Rieke-Zapp · M. Schwab
Institute of Geology, University of Bern, Bern, Switzerland
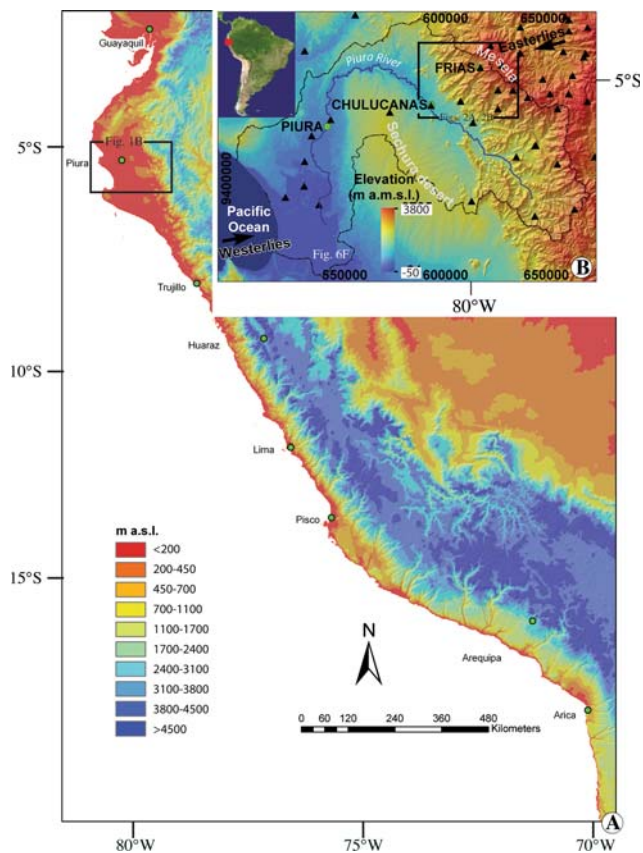e-mail: fritz.schlunegger@geo.unibe.ch

Fig. 1 a Morphology of the western escarpment of the Peruvian Andes and location of the Piura drainage basin in the north at 5°S latitude. **b** Details of the Piura drainage basin. *Green circles* show the relevant populated centers (Piura, Chulucanas and Frias), and *black triangles* correspond to precipitation gauging stations. The drainage basin limit is shown by the *dashed line*. The figure also shows the location of the photo illustrated in Fig. 6f. Note that the Meseta on the cordillera is characterized by a flat surface at ca. 3,700 m a.m.s.l. and marks the upper boundary of the headwaters. Towards the Sechura desert, an arrange of parallel and west facing drainages feed the main axial drainage system that is referred to as Piura River. This river ends at the mudflat or in the terminal lake during Bolivian High and El Niño, respectively. Note that evaporites are found in the proximity of the terminal lake. Elevation model, US Geological Survey (2006). Source for this dataset was the Global Land Cover Facility. Coordinates and projection is UTM Z17S WGS84

identify potential relationships between the pattern of precipitation rates and the landscape's architecture from a general point of view. This is done by comparing the modern pattern of precipitation rates with (1) data about sediment and water flux of the trunk stream, (2) field-based geomorphic observations, and (3) morphometric parameters extracted from digital elevation models. The scope of the first step is to identify, from a broad perspective, how climate has imprinted the mountain landscape in this part of the Andes. In the second step, we will explore how the landscape near Piura potentially responds to higher-than-average precipitation rates. In particular, we will determine

the locations of enhanced erosion during the 1997–1998 El Niño period. This is accomplished using SAR intensity data of four Single Look Complex (SLC) scenes that were registered in late 1997 and early 2002 and thus enclose the 1997–1998 El Niño event. These images have a ground resolution of 30 m. They record the phase (time delay) and amplitude (energy intensity) of microwave echoes returned from Earth's surface. We select SAR intensity difference data because SAR amplitudes (energy intensities) are sensitive to roughness patterns of topographies (Smith 2002). This implies that any large-scale modifications in the surface roughness caused by e.g., gullying, dissecting, and landsliding are expected to yield a distinct pattern of intensity change that we intend to detect here.

Local setting

Geology

The Andean western slope is the result of the subduction of the Nazca oceanic plate beneath the South American continental plate (Jaillard et al. 2000). Collision was initiated in the Early Jurassic and has continued up to the present (Ramos and Aleman 2000). Low temperature thermochronometric data from Peru yield exhumation rates of approximately 200 m My^{-1} since the Late Miocene (Wipf et al. 2008).

The Northern Peruvian segment where the Piura region is located lies on a flat-slab subduction zone. Here, the subduction of the aseismic Carnegie ridge has resulted in one of the lowest seismicity segments in the Andes (Pilger 1981). The bedrock comprises Cretaceous intrusive rocks, Paleozoic metasediments and Tertiary volcanoclastics in the Sierras. The coastal regions are made up of Precambrian high grade rocks, and Quaternary fluvial, shallow marine and eolian deposits (Cobbing et al. 1981).

Climate

In the Sierras, precipitation falls annually during the Bolivian High between December and February, being particularly abundant during La Niña (Garreaud and Aceituno 2001). Along the Peruvian coast, climate is influenced by the Peru Current and coastal upwelling (Toggweiler et al. 1991). Furthermore, the contrast in temperature and pressure between the eastern and western Equatorial Pacific drives the Pacific Walker Circulation cell with an ascending branch of moist, warm air over the Indonesia low and sinking motion over the eastern Pacific (Reynolds and Smith 1995; Bjerknes 1969). The result is a persistent cold and dry high-pressure climate along the coast of South America (Curry and Webster 1999). The

cold air is capped by the thermal inversion located between 600 and 1,500 m a.m.s.l, precluding the development of convective precipitation (Barry and Chorley 1998; Woodman 1998).

Every 2–10 years, around late December, a substantial warming in the sea surface temperature (SST) occurs offshore Southwestern Ecuador, Peru and Northern Chile, signaling the presence of El Niño. This enhanced seasonal warming marks the culmination of the large-scale warm phase of the ENSO cycle with SSTs at or above 25°C. Excessive and severe rainstorms may be the most direct consequences of El Niño, causing disastrous damages to human infrastructure and agriculture (Philander 1983; Goldberg et al. 1987; Horel and Cornejo-Garrido 1986). This was particularly the case in 1983 and 1998 for the Piura region where the El Niño phenomenon resulted in large-magnitude floods.

El Niño-like conditions have been well documented by several authors during the geological past (Ravelo et al. 2004; Huber and Caballero 2003; Wara et al. 2005). These studies show that El Niño-like situations reached a permanent state during the Pliocene Warm Period. This implies that similar forces have been influencing the climate along the Peruvian coast since geological time scales, at least since the closure of the Panama Isthmus (Coates et al. 1992).

Precipitation pattern, hydrology and sediment discharge

The precipitation pattern is based on a 30–40 years long survey at ca. 50 gauging stations covering ca. 11,000 km^2 (Fig. 1b). During 'neutral' or 'normal' periods, precipitation falls in the austral summer. Under these conditions, moisture is carried by the easterlies, crossing the Amazon basin and releasing up to 1,300 mm of rain per year in the eastern flank of the Sierras at ca. 3,500 m above sea level (Fig. 2a). Precipitation accumulation then decreases to zero towards the Sechura desert close to the Pacific. In contrast, in 1983–1984 and 1997–1998, which were El Niño periods with strong anomalies in the rainfall pattern, the precipitation is influenced by both the easterlies in the Sierras and the westerlies at coastal low levels (Fig. 2b). During these periods, the Sechura desert (e.g., the station at Chulucanas, Fig. 2c) received up to 4,000 mm of precipitation accumulation between December and June (e.g., El Niño 1983). This corresponds to an enhancement of precipitation accumulation by several orders of magnitude compared to 'normal' or 'neutral' years. Towards the Sierras (e.g., station at Frias, Fig. 2c), precipitation totals continuously decreased to ca. 1,500 mm during the same period. Hence the contrast in precipitation accumulation decreased to less than onefold. At the Piura gauging station, the impact of this dual climate pattern was seen in high magnitudes of water and sediment discharge, respectively (Fig. 3).

Step 1: assessment of the geomorphology and the nature of sediment transport in general

The headwaters of the Piura River comprise ca. 10 predominantly transverse drainages. They are located in the Sierras with elevations up to 3,600 m above sea level (Fig. 1). These transverse drainages that are ca. 50 km^2 large on the average discharge into an axial drainage. During 'normal' or 'neutral' years the major channel is mostly dry because a large portion flows as ground water, and because water is also used for agricultural purposes. During flood stage (El Niño) the channel experiences surface runoff and shows a distinct meandering pattern with laterally migrating meander belts. This was particularly the case during the 1982–1983 and 1997–1998 El Niño periods (Fig. 4). Beneath Piura the river ends in a mudflat and finally in a terminal lake that is referred to as La Niña by the local community (Fig. 1b) and is unrelated to the climatological effect of the same name.

In recent publications, Schneider et al. (2008) used geomorphic maps and morphometric data to reconstruct the nature of surface erosion and sediment transport in the Piura drainage basin. According to these authors and observations in the field, the headwaters and the transverse tributaries of this drainage basin comprise three areas that differ in regolith thickness and intensities of weathering, the nature of surface erosion and sediment transport, and the drainage architecture (Fig. 5). The Meseta (Fig. 6a) with an elevation altitude of approximately 3,600 m above sea level forms the top of the transverse drainages. There, the bedrock is mantled by a >10-m thick cover of unconsolidated material that forms m-thick successions of amalgamated floodplain/palaeosoil sequences. In some locations, the regolith is deeply dissected by gullies (Fig. 6b) that are several meters deep, tens of meters wide and hundreds of meters long. The upper terminations of these gullies are abrupt with pronounced headwalls indicating that headward propagation of the gullies was accomplished by groundwater sapping. Note that the gullies are generally coupled with the channel network.

The second area comprises the portion between the Meseta and the region beneath the town of Frias with an elevation of approximately 1,500 m above sea level (upper segment of Fig. 5b). In this area discharge is directed towards the southwest. There, the uppermost border displays an amphitheatre-shaped concavity with diameters of approximately 5 km width (Fig. 5) and slopes that are up to 60° steep. The upper termination of the headwaters is

Fig. 2 Seasonal and 1993–
1998 (El Niño years) influence
in the pattern of precipitation.
The influence of seasonal and El
Niño climate is observed as an
overlap in the precipitations
rates. *Black triangles*
correspond to selected
precipitation gauging stations,
green circles are the relevant
localities in this study. **a** An
average of 25 years of
precipitation on the west flank
of the Andes during non-El
Niño years. **b** Average
precipitation related to El Niño
1983 and 1998. The absence of
error bars indicate that only one
complete year was available
(either 1983 or 1998). *Dashed
lines* show the ratio between El
Niño/non-El Niño
precipitations-period.
Coordinates and projection,
UTM Z17S WGS84. The data
are taken from the Chiara–Piura
project, Piura, Peru (Anuario
Hidrologico, Ministerio de
Agricultura, Piura). **c** Contrast
in precipitations rates across the
western flank of the Northern
Andes, with precipitation at
Frias in the upper segment
during 1985 (neutral) and El
Niño 1983, and precipitation at
Chulucanas in the lower
segment (upper limit of the
Sechura desert) during 1985
(neutral) and El Niño 1983
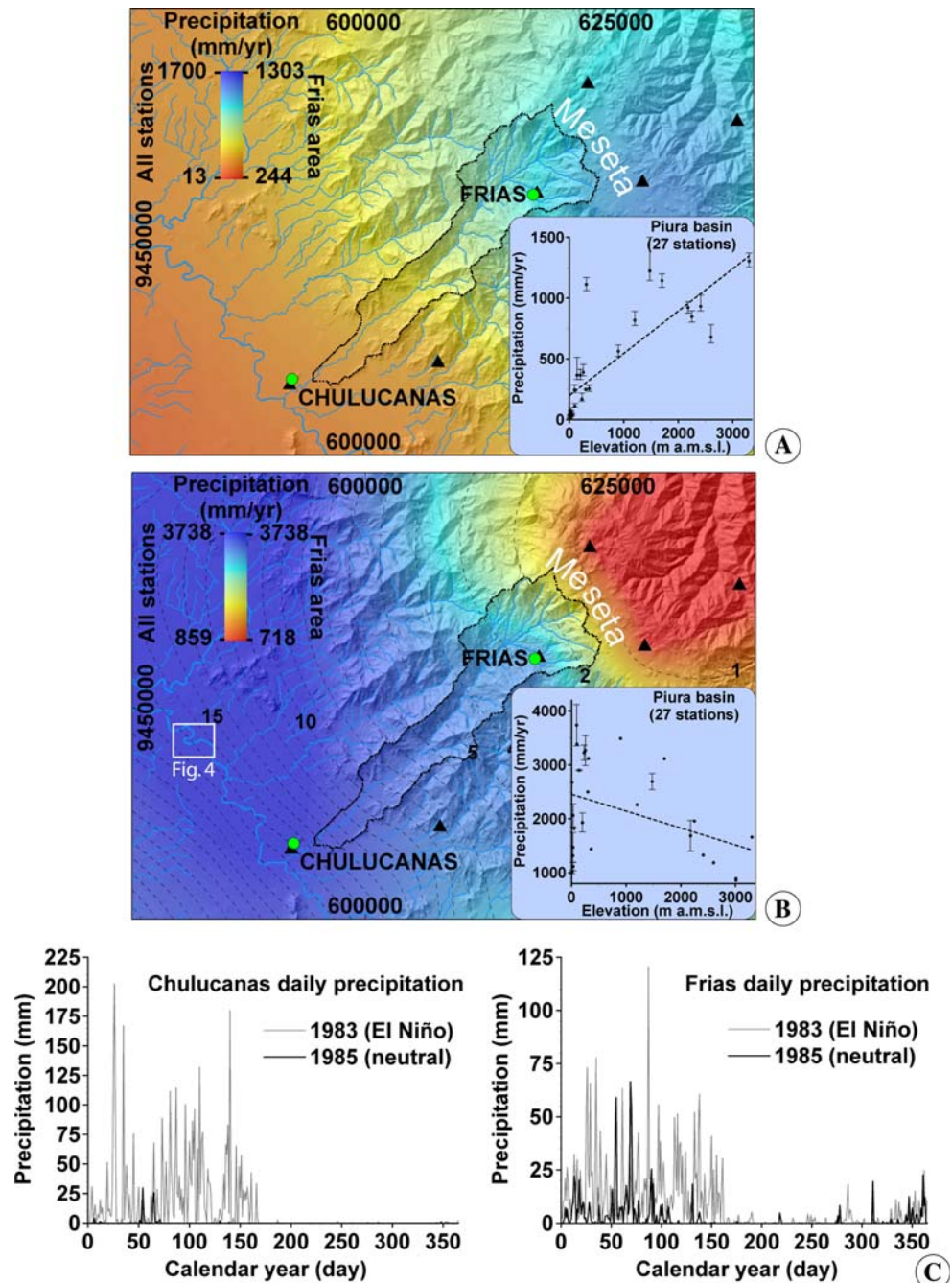
defined by a sharp scarp-line, which—at closer inspec-
tion—is made up of coalescing concave geometries. These
features were considered by Schneider et al. (2008) to have
been formed by landsliding (Fig. 6c). Also, this upper
segment displays multiple gullies several hundreds of
meters wide and several tens of meters deep with abrupt
and pronounced headwalls (Fig. 6d, e). These geomorphic
features are interpreted by the same authors to have been
formed by groundwater sapping, seepage erosion and
associated mass wasting processes (Fig. 5a). Mass move-
ments were the origin of granular flows that are a common

sediment transport mechanism in this part of the Andes.
Because these erosional processes have only affected the
regolith, and since exposure of bedrock is rarely observed,
Schneider et al. (2008) assigned a transport-limited sedi-
ment flux regime to the channel network in this uppermost
segment.

The lower segment of the transverse drainages (Fig. 5b)
comprises the foothill of the Sierras and the eastern border
of the Sechura desert. There, hillslopes are characterized by
a <1-m thick regolith cover and the frequent exposure of
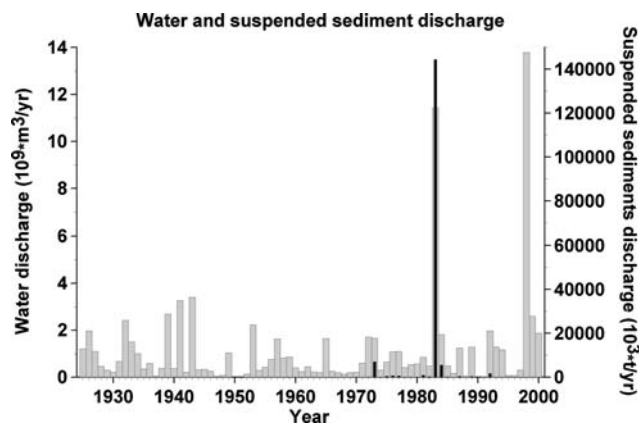bedrock. Also in this segment, the channel network on

Water and suspended sediment discharge

Fig. 3 Water and suspended sediment discharge at Piura. *Gray bars* correspond to total yearly water discharge from 1925 until 2000, *black bars* correspond to yearly suspended sediment discharge, both at Piura city. Continuous measurements of suspended sediment were carried out from 1972 until 1992 and later during El Niño 1998. Note that the increase in sediment discharge during El Niño 1998 was consistent with the increase in water flux, but due to the magnitude of the flux, only a few measurements were taken. The data are taken from the Anuario Hidrologico, Ministerio de Agricultura, Piura

hillslopes is made up of bedrock channels with an ephemeral runoff especially during El Niño periods (Fig. 6f). Occasionally, the channel floors are mantled by a m-thick cover of sand and gravel. The deposits reveal a clast-supported fabric that lacks a sedimentary matrix. These features suggest that sediment transport has been accomplished by episodic granular flows. In contrast to the upper segment, the frequent occurrence of bedrock channels suggests that sediment flux in the channel network has been supply-limited to a large extent.

The axial drainage is the meander belt of the Piura River (Fig. 1b). It comprises approximately 30–50 m wide and >5-m deep trunk channel that is laterally bordered by a several hundreds of meters-wide floodplain. Satellite TM-images show that lateral shifts of the meander belts have occurred mainly during flood stage, i.e., during periods of El Niños (Fig. 4). Towards the Pacific coast, the axial drainage is bordered by a presumably Pleistocene dune field (Fig. 1b) that is currently covered and stabilized by trees. This dune field marks the transition between the Sierras and the Sechura desert. The latter environment (Fig. 6e) also hosts the terminal lake of the Piura River. The bedrock of the Sechura desert is made up of uplifted Pleistocene shallow-marine sandstone deposits (Fig. 1b) that are generally parallel laminated. Some sandstone units display trough-crossbedding with mm-thin mudstone layers between the sandstone laminae. These features indicate that waves and tides were the most important processes for sediment transport in this particular environment. In between the uplifted Pleistocene deposits, flooding of the Piura River and succeeding desiccation has resulted in the
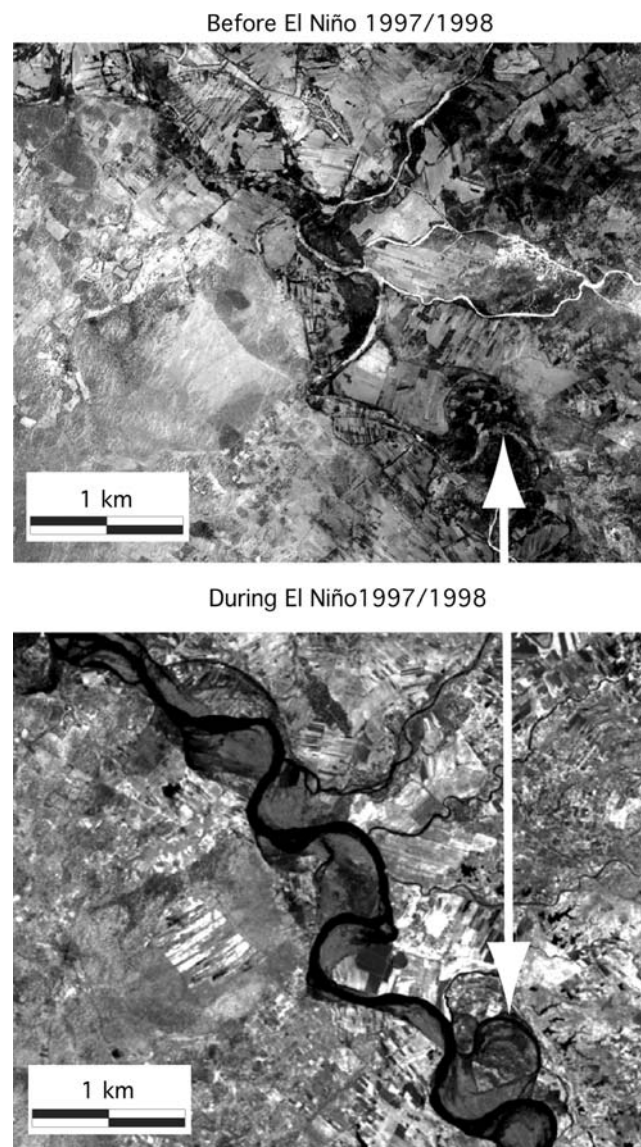

Fig. 4 Orthophotos, showing flow pattern of the Piura River before and during the 1997–1998 El Niño period

establishment of a modern sand- and mudflat that is referred to La Niña terminal lake (Fig. 1b). The deposits display salt crusts with multiple teepee desiccation structures (inset of Fig. 6e).

Step 2: assessment of the landscape response to the 1997–1998 El Niño event

We use synthetic aperture radar (SAR) intensity images to identify the locations where substantial changes, like landsliding and gullying occurred during the 1997–1998 El Niño episode. The images were acquired by the ESA satellite ERS-1 and ERS-2 that operate in C band (56.6 mm
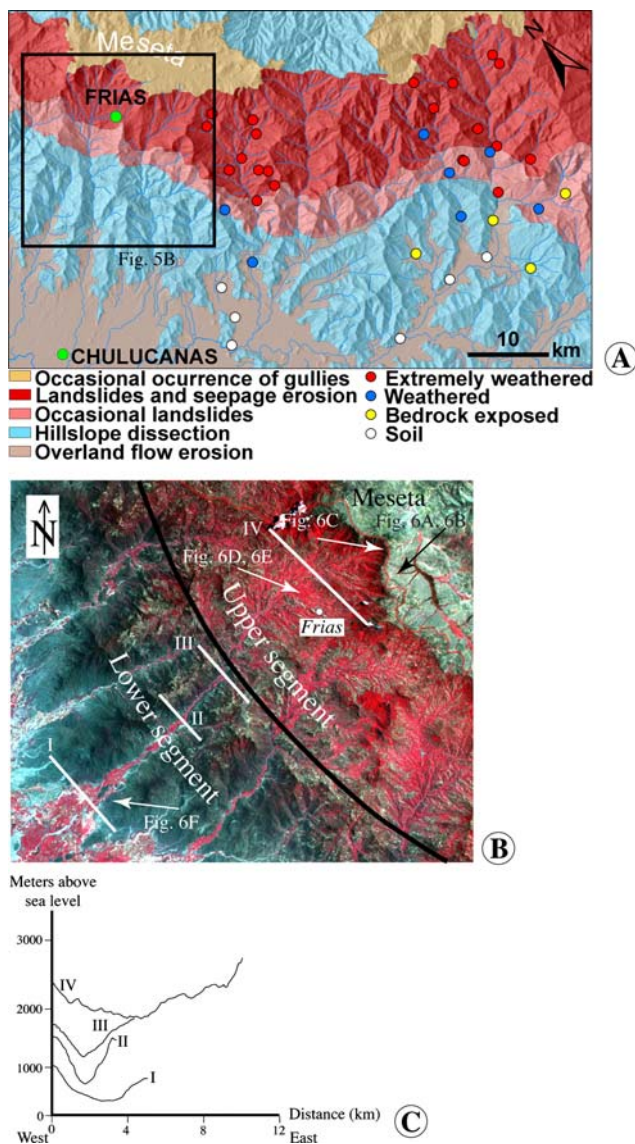
Fig. 5 a Geomorphological map of the western flank of the Northern Andes. **b** Landsat ETM + 7, US of the transverse drainage sourced from the Frias area. Note that the transition from the higher to the lower segments is readily visible by the vegetation pattern. **c** Topographic cross-sections of the Frias tributary. The figure also shows the locations of the photos illustrated in Fig. 6

wavelengths). In the next sections we present a short summary of the SAR intensity technique.

General aspects of SAR technology

Introduction

Synthetic aperture radar systems are active satellite sensors working with microwaves, consisting of a signal emitter of microwave radiation and a receiver (Lillesand and Kiefer 2003). Microwaves penetrate clouds without substantial

distortions and are not subjected to multiple atmospheric scattering as visible light is (Albertz 2007). For the case of the ESA satellites, the microwave radiation is emitted in short pulses with a wavelength of 56.6 mm, polarization (VV) and a look angle of 23° perpendicular to the azimuth. The signal is reflected from the surface and received by the antenna on the satellite platform and registered in terms of polarization, phase and amplitude. The last two parameters are the components of a 'complex SAR image' (Smith 2002). Note, however, that the interaction between the transmitted wave and the surface does not only result in reflection. Specifically, due to the roughness of the surface, or due to the transmission into the first thin layer of the soil, the receiver records the backscattered portion of the transmitted signal (Smith 2002). Note also that during the reflection and the passage through the atmosphere the microwaves change their phase, amplitude and polarization.

On the satellite platforms SAR images are formed by registering the phase (time delay) and amplitude (energy intensity) of microwaves that were echoed from the Earth's surface. If two radar images are available that were taken at different times and if the positions of the SAR antenna are identical (i.e., the length of baseline is zero), then any change on the Earth's surface between the times of the first and second images will introduce a small distortion of round-trip distance, causing an offset in the phase (Zebker et al. 1994). This offset is readily seen by subtracting one phase image from another, yielding a map of interferometric phase known as an interferogram that can then be converted to the displacement of the surface (e.g., landslides, Fruneau et al. 1996). However, if the baseline is greater than zero, then the calculated interferograms also comprise the 3D effect of the topography. In this case, the topographic and displacement contributions to the interferogram must be separated from each other before the displacement map can be calculated. This requires independent information from the static topography, for which a synthetic interferogram will be modeled (scaled with the baseline) and subtracted from the measured one (e.g., Fruneau et al. 1996).

The analytical steps outlined above require a robust correlation between the two acquired images. For the situation where the time span between image acquisitions (temporal baseline) exceeds several months, the images cannot be correlated, and the coherence loss (or decorrelation) precludes interferogram construction (Smith 2002). This is certainly the case for the situation presented here where images enclosing the 1997–1998 El Niño event were only available for late 1997 and 2002. Accordingly, we use the amplitude components (intensity) of the SAR images that image the general pattern of surface reflectivity in the C band (Fig. 7a, b). It is important to note, that while the
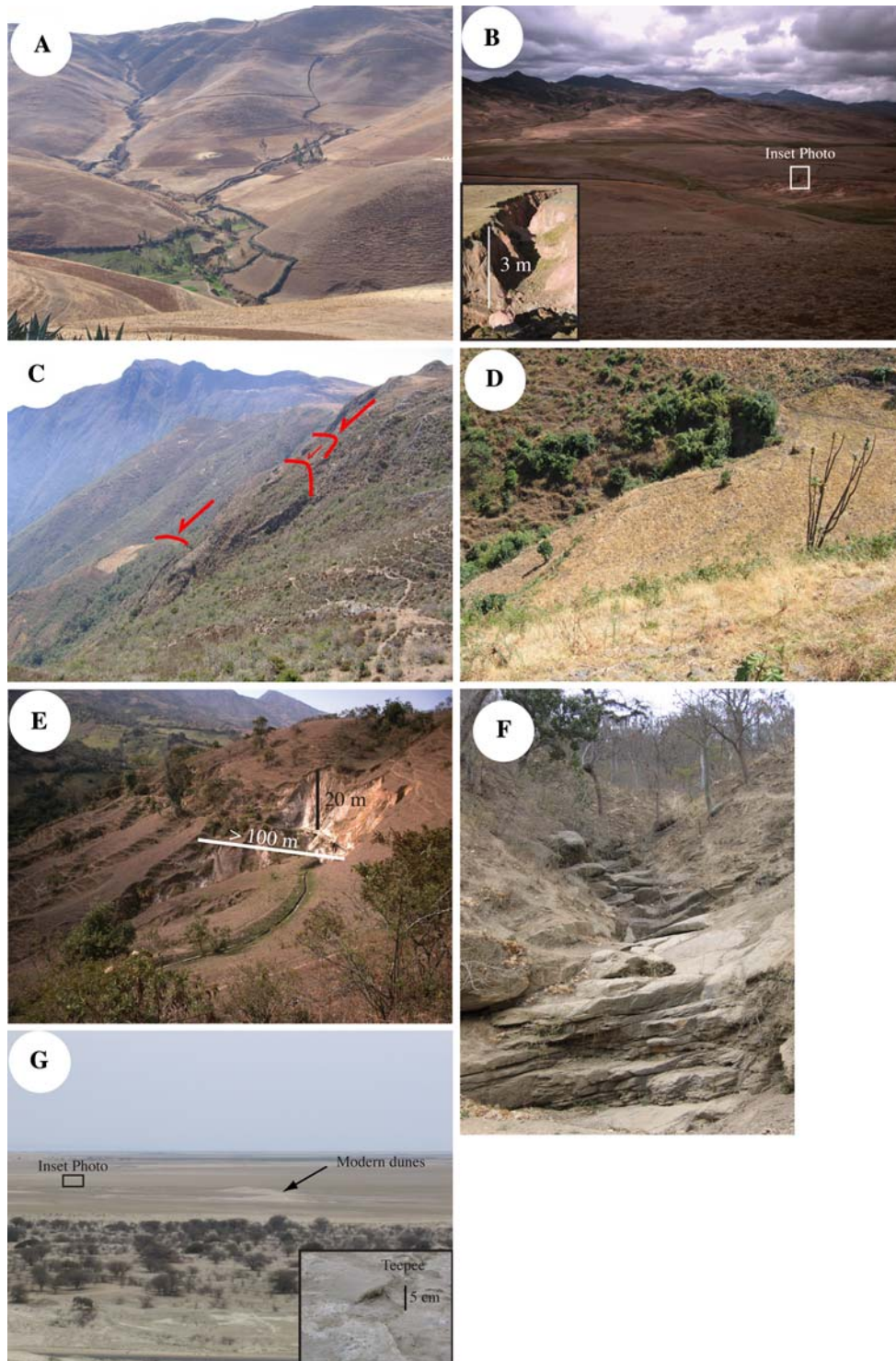
Fig. 6 Photos from the field showing (**a**, **b**) the landscape of the Meseta with several meter deep gullies, **b** gullies affecting the regolith in the upper segment beneath the Meseta, **c** escarpment with slide-blocks, (**d**, **e**) are examples of gullies, **f** illustrates a bedrock channel, and **g** the situation of the Sechura desert. Debris flow channel in the lowermost segment. See Fig. 5 for locations of photos, and Fig. 1b for location of photo (**f**)

intensity images may show a strong visual similarity to maps of the local topography, they are not exact representations thereof. Reflectivity is determined by a number of factors besides local topography and surface roughness, such as vegetation, moisture content of the soil, exposure of bedrock, variations in lithology and angle of incidence

Fig. 7 Maps of intensity of the reflected radar signals, before (**a**) and after (**b**) the 1997–1998 El Niño period, differences in local mean of intensity (**c**) and local variance of intensity (**d**). Sub-image (**e**) is same map as sub-image (**b**), but shows the areas of substantial changes in the radar signals (*red dots*). Coordinates are UTM Z17S
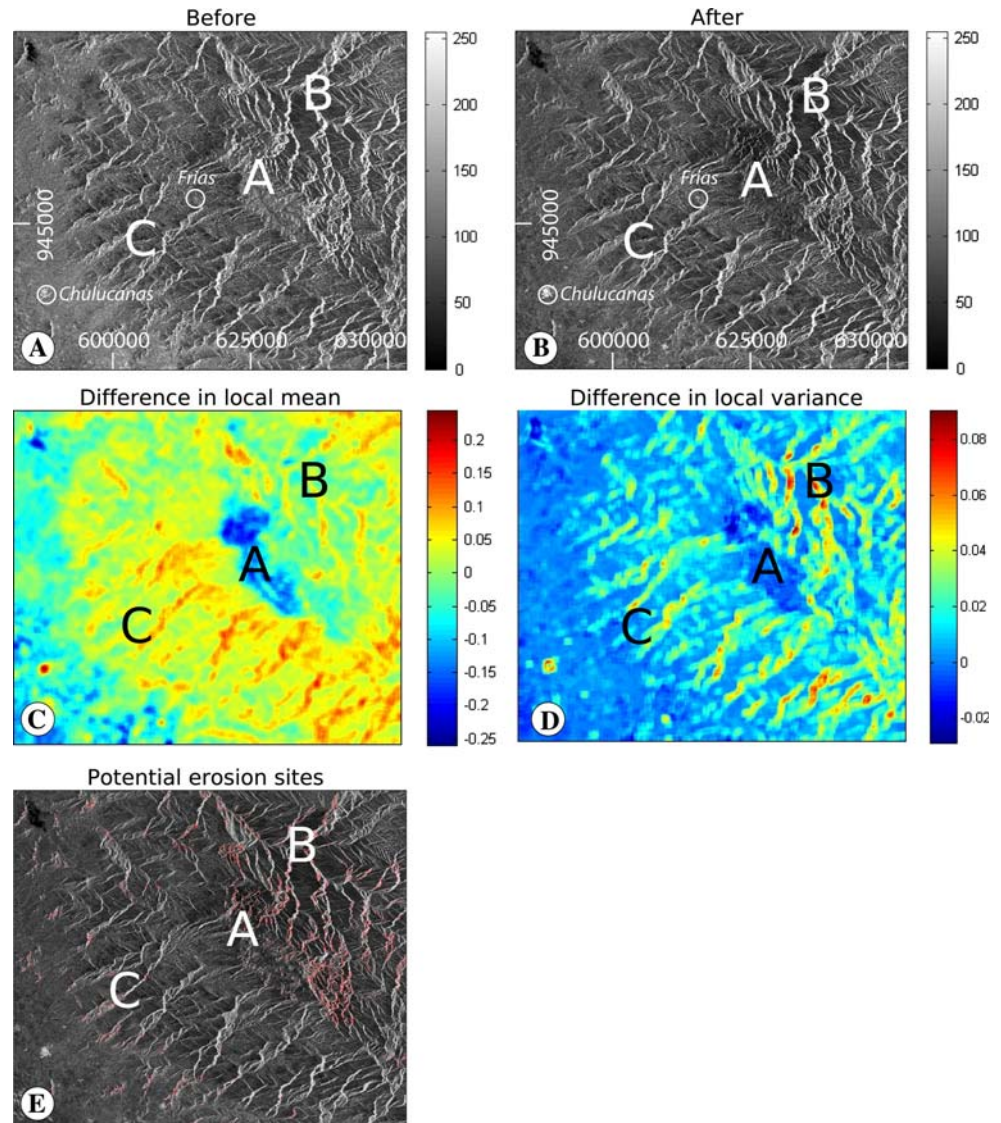
of the signals with regard to the slope of the surface. When comparing the two intensity images, any changes in reflectivity will result in a distinct pattern of intensity differences.

Difference in SAR intensity and variance

In this section we focus on a practical geological aspect of the SAR application. For a technical description of SAR the reader is referred to Henderson and Lewis (1998) and Oliver and Quegan (2004). Here, multitemporal SAR intensity images were used to detect the regions that have experienced focused erosion (e.g., landsliding, gullying, dissection) during the 1997–1998 El Niño period. The use of SAR intensity images is based on the concept that a signal has the identical intensity pattern of response if no change in overall reflectivity has occurred between the

acquisition times. Further, any substantial changes in intensity have a fair chance of being caused by changes in surface roughness in relation to e.g., focused erosion (Ulaby et al. 1986). Changes in reflectivity between the acquisition times of the two images can, however, have a wide range of causes, not all of which are directly or indirectly connected to erosion processes (Ormsby et al. 1985). Some possible changes include (1) change in vegetation (either natural or anthropogenic, i.e. clearing), (2) change in moisture content (e.g., due to seasonal variations or weather), and (3) differences in angle of incidence between the two images. Therefore, the assignment of a landscape change to a specific process causing that particular modification requires a calibration by visual observations. This will be accomplished in this paper through the use of high-resolution aerial photographs of the affected areas.

The variance of SAR intensities between neighboring pixels can also be used as an indicator for surface roughness or a change thereof when comparing SAR scenes of different epochs. Consequently, we anticipate that segments within a landscape that have been strongly modified by landsliding and gullying are identified with the SAR technology by a difference in both the magnitude and the variance of intensities.

Application of the SAR technique to the Piura drainage basin

Analytical steps

Four single look complex (SLC) scenes were selected for analysis of effects related to the 1997–1998 El Niño event. Hence we analyzed images taken in late 1997 and early 2002. The SLC scenes including estimation of range and azimuth offsets were processed using GAMMA Software (Crosetto et al. 2005). Note that because no sediment was transferred in the Piura River during 'normal' or 'neutral' years following the 1997–1998 El Niño period (Fig. 3), we anticipate that no significant landsliding, gullying and/or dissection occurred after this particular El Niño episode. Hence, any changes detected between the 1997 and 2002 images can be related with confidence to the strong precipitation rates during the 1997–1997 El Niño.

To ensure the consistency between pixels in the correlation, a rigorous calibration between the SAR images was performed to guarantee a sub-pixel co-registration level. An initial offset (base line) between the SAR scenes was estimated based on the orbit parameters. Two iterations of the initial range and azimuth offsets between the scenes were carried out. To avoid ambiguity problems with the second iteration, the first one is made with multi-look subsamples and later in single look. Both iterations were performed based on a two dimensional cross correlation function. This was calculated using the peak of the function to yield the initial offset. After the second estimation, a signal to noise ratio (SNR) correlation is calculated to estimate the confidence in the offset.

The result of these two iterations is used as a base for the estimation of the range and azimuth registration offset fields. This is done by calculating a cross correlation optimization of the scenes. This requires the use of an intensity tracking algorithm. These results were finally utilized to calculate and register the offset polynomials based on linear least-squares adjustment. The polynomials are of fourth order and include an average deviation filter. The final registration was accepted if the misfit did not exceed 0.2 pixels (Table 1).

After the polynomials were calculated, they were used to co-register the SAR scenes. A range spectrum filter was applied to compensate the spectral shift induced by the slight difference in incidence angle between the scenes, retaining only the range spectrum interval common to both scenes. The resample process was performed using a weighted sine cardinal (sinc) interpolation kernel. Multi-look subsets were calculated with 1 range looks and 5 azimuth looks, using the complex input values from the SLC

Table 1 Offsets and correlation between before and after El Niño SAR scenes

SAR pair	19971612335803717–20002601249293717	19971612335803699–20002601249293699
Initial offsets (range; azimuth)	−13;910	−13;959
First estimated offsets (multi-look), (range; azimuth; SNR correlation)	−13.317; 892.963; 56.489	−14.192; 950.862; 74.990
Second estimated offsets (single-look), (range; azimuth; SNR correlation)	−13.616; 893.559; 24.823	−14.259; 951.511; 26.051
Offsets above SNR threshold = 7, 128 × 128 window size	582 out of 1024	725 out of 1024
Offsets above SNR threshold = 7, 128 × 128 window size, using intensity cross correlation	19,000 out of 31,878	25,610 out of 33,516
Final accepted offsets for polynomial coefficients	Final solution: 17,965 out of 31,878	Final solution: 24,820 out of 33,516
Final range offsets polynomials ($a0 + a1*x + a2*y + a3*x*y$)	−12.26495, −6.39022e−04, 2.78812e−05, −1.64337e−09	−12.73509, −6.84097e−04, 1.38954e−05, 1.69836e−09
Range polynomial coefficients error ($a0 + a1*x + a2*y + a3*x*y$)	2.22080e−04, 7.73921e−08, 1.39515e−08, 4.49460e−12	2.42021e−04, 8.57560e−08, 1.54011e−08, 5.55202e−12
Final azimuth offsets polynomials ($a0 + a1*x + a2*y + a3*x*y$)	894.23610, −4.04707e−04, 1.13480e−05, −3.52568e−09	952.18764, −4.23241e−04, 7.98795e−07, 2.12661e−10
Azimuth polynomial coefficients error ($a0 + a1*x + a2*y + x3*x*y$)	9.71386e−04, 3.38515e−07, 6.10245e−08, 1.96595e−11	1.23272e−03, 4.36795e−07, 7.84450e−08, 2.82790e−11

Accepted samples are <0.2 misfit pixels. This table also shows the final range and azimuth error polynomials

scenes. Here real values of multi-look intensity images were calculated.

The resulting intensity images (Fig. 7a, b) were projected to UTM coordinates using the WGS84 ellipsoid, zone 17 South. No terrain correction was made to keep the original equivalence that was calculated by co-registration of the scenes. The geocoding process was achieved applying a backward transformation thereby using a previous created look-up table. In this way, a table with the corresponding coordinates is created for each point in the SAR image.

Calculation of differences in intensity and variance

Differences in linear means and local variances (Fig. 7c, d) of the intensity images were determined as a measure of the variations in intensity responses. The intensity difference (Fig. 7c) is determined by calculating the linear difference between the two images (Fig. 7a, b) after normalization to the reflectivity of the town of Chulucanas. We justify this approach by the assumption that the average reflectivity of the urban area would not have changed significantly between the acquisitions of the images.

For the assessment of the differences in local variance (Fig. 7d), the local averages of intensities need to be known. Accordingly, for each pixel of the individual images, we determined the average by considering the intensities of the neighboring areas within a radius of eight pixels. Note that this method can lead to artifacts and edge effects near the map boundaries. Also note that the same process was applied with a radius of four pixels without revealing a significant change in variance pattern. The most notable difference is the slightly larger smoothing effect obtained by choosing a larger radius.

The difference maps of Fig. 7c, d were then reduced to a binary image showing 'significant' changes in intensity and variance on the map. It must be noted that both strong increases and strong reductions in intensity and variance are interpreted as possible changes in local topography and/or surface roughness. The cutoff values for 'significant' change were chosen in an arbitrary manner at 10% absolute change in local mean and linear difference, and at 5% absolute change for the local variance. Multiplying these resulting binary maps in an element-by-element fashion produces a new binary map highlighting areas of general change. This image served as a mask to highlight the affected areas on the second original intensity image (Fig. 7e).

Finally, the field-based calibration of the map showing the general pattern of change is accomplished using tools of aerial photogrammetry. Specifically, the map of Fig. 7e was overlain in Google Earth® at a transparency setting of 40% opacity. The town of Chulucanas and the distinctive hill to the south of the town provided the references to

rotate and zoom the image to the best possible fit. These two features were chosen due to their proximity to the area with the highest resolution of visual band images available in Google Earth®. The fit is not perfect, and the correlation between the photography and the overlay degrades with increasing distance from the town.

Results and interpretation

Intensity difference and variance difference pattern

Figure 7a, b illustrates the co-registered SAR scenes for the situation before and after the 1997–1998 El Niño event. In these images, the bright linear features in the reflected radar signals correspond to trunk and tributary channels, ridges with exposed bedrock, and to transitions from shrubs to forests. Note that this assignment is based on field observations and investigations of visual band satellite photographs provided by Google Earth®. Figure 7c, d displays the pattern of the differences in local mean intensity, and intensity variance, between the two images after normalization to the reflectivity of Chulucanas (performed as mentioned above).

Most important purpose of this paper, however, is the pattern displayed on the map of Fig. 7e which allows the detection of locations that experienced a change in both the magnitude and the variance of the local radar intensities. Note that the combination of both the local mean and local variance will filter out systematic and large-scale effects that may be due to vegetation changes or to a different angel of incidence. The map of Fig 7e allows the delineation of three segments that differ in the pattern of magnitude and variance change. The Meseta, marked as area A in the images, shows a strong negative change in local mean reflectivity, but almost no change in local variance. This could be explained by the area having a fairly high roughness at a local scale (Fig. 6a), which results in a strong intensity change if the radar signals had different angles of incidence, which was presumably the case here. Area B is located in the mountainous region to the north–east of the Meseta, where a network of deeply dissected channels is visible (Fig. 1b, Schneider et al. 2008). This segment shows high magnitudes in the local mean difference map (Fig. 7c), and even higher values in the local variance difference map (Fig. 7d). This results in a high density of 'points of interest' (red dots) in the combined difference overlay (Fig. 7e). Unfortunately, the currently available visual band imagery of this area is of limited resolution which hinders a calibration with field-based information. Area C finally is located between the Sechura desert and the Meseta, and consists mainly of the southwest-oriented tributary systems of the Piura River.

Similar to region B, the hillslopes especially in the lower segments of these tributaries are deeply dissected by tributary channels (see above, and Fig. 5). However, in contrast to region B, the density of locations with strong local changes in intensity mean and intensity variance (red dots) is not quite as high. However, the quality of visual band imagery is far superior, enabling us to calibrate the combined difference overlay of Fig. 7e with field-based information. This will be done in the next section.

Calibration of intensity difference pattern

The combination of the intensity difference data and the satellite photographs and terrain model of Google Earth® yields a precise calibration of the segments that experienced both a substantial change in local mean and variance of intensity. An overview of the area, including a semi-transparent overlay of the intensity change data, is shown in Fig. 8. Insets (Fig. 8b–f) are taken from regions where high-resolution imagery data are available. They present close-up views showing evidence for substantial intensity change. Interestingly, these regions exhibit fresh scars and are dissected by bedrock channels with sharp lateral boundaries. These features indicate the occurrence of recent landscape refreshments by erosion. Because the gauging station at Piura implies no substantial sediment export after the 1997–1998 El Niño event (Fig. 3), we relate the erosional scars on Fig. 8 to the higher-than-average intensity rainfall event in 1997–1998. Accordingly, we interpret that the differences in the local mean intensity and variance of the radar signals especially in the southwest-oriented tributaries of the Piura River most likely represent the landscape's response to the 1997–1998 El Niño precipitation event. Indeed, during 'normal' or 'neutral' years, the magnitude and intensity of precipitation is presumably too low (Fig. 2) to initiate hillslope-clearing debris flows as seen on the examples of Fig. 8.

Discussion

Relationships between climate and landscape morphology in general

We interpret the differences in the nature of sediment transport and erosion, and in the morphometric properties to reflect the combined effect of the easterlies and the anomalous precipitation in relation to El Niño. First, the
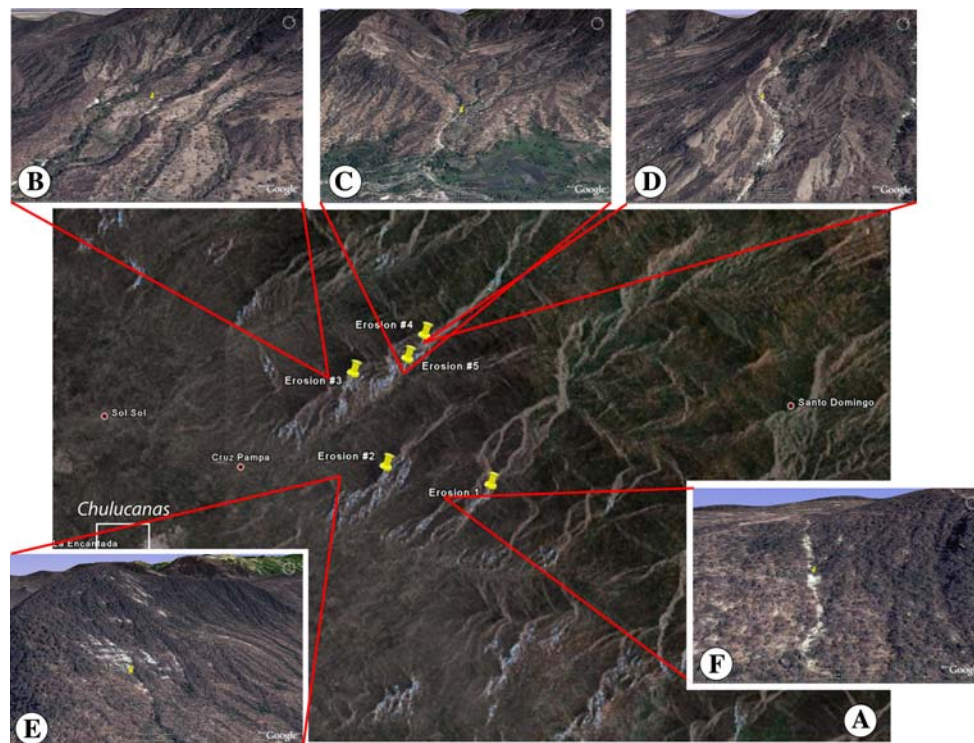

Fig. 8 The main figure (**a**) shows a section of the overlay used in Google Earth®, consisting of the area-of-interest map shown in Fig. 7e, projected onto the Quickbird, high-resolution visual band imagery of the region and the local topography model. *Insets* (**b**–**f**) are detail images (visual band images used in Google Earth®) of five examples of strong erosion, determined as regions of interest, labeled 'Erosion 1' through 'Erosion 5'. All five examples are located in the hills north–east of Chulucanas, in the area marked by hillslope dissection in Fig. 5. (QuickBird©DigitalGlobe, 2008; Distributed by Eurimage)

change from transport- to supply- and weathering-limited status in sediment flux occurs at the same altitude at which the influence of El Niño becomes enhanced, i.e., between the upper and lower segment of the transverse drainages (Fig. 5b). It is likely that in the higher portion, the monsoonal pattern of precipitation related to the Bolivian High (Grimm et al. 2005) promotes the formation of sediment by weathering (Birot 1968) as indicated by the presence of a several m-thick regolith that covers the entire landscape. In this region, the production rates of sediment by weathering potentially exceed rates of sediment transport in the channel network.

Further down, at the foothills of the Sierras and the border of the Sechura desert, the presence of debris flow channels on hillslopes exposing bedrock implies an episodic and a supply-limited flux of sediment. This is the segment where high contrasts in precipitation rates related to El Niño have been measured (Fig. 2). This change in the nature of sediment transport and erosion in channels (Fig. 5a) is interpreted here to result from the high ratio between large- and small-magnitude floods in relation to episodic precipitation during El Niño. The rational behind this argument lies in the observation that a river needs to transport its bedload before the bedrock becomes eroded, and that critical flow strengths must be exceeded to remove this bedload (Molnar 2001). It appears then that the large floods during periods of strong El Niños increase the magnitudes at which these critical thresholds are surpassed, which, in turn, results in efficient sediment transport and erosion. The pattern of climate driven by El Niño thus promotes sediment transport in channels to the extent that the transport capacity exceeds supply rates of sediment by weathering on hillslopes.

We also interpret that episodic precipitation in the lower portion of the drainage basin potentially promotes headward erosion and growth of the drainage basin. Specifically, in the headwaters, the amphitheatre-like concavity of the landscape and the sharp scarp-line defined by the eastern termination of the catchments implies headward growth of the drainage basin by landsliding (Hovius et al. 1998; Strasser and Schlunegger 2005). Headwater propagation of drainage basins, however, only occurs if the capacity of channelized processes to export sediment exceeds sediment supply rates. It was interpreted above that efficient export of sediment could potentially be attributed to El Niño. Hence, anomalous precipitation during El Niño periods tends to result in efficient lowering of valley floors, thereby increasing the local relief, promoting headward erosion and initiating further landslides.

Landscape response to the 1997–1998 El Niño event

It is interesting to see that in the southwest-oriented tributaries of the Piura River, focused erosion related to the 1997–98 El Niño occurred on those hillslopes that are bound to, and therefore linked with, the channel network (Fig. 8). This is especially the case for the hillslopes in the lower segments that are dissected by debris flow channels (Fig. 5a). In these segments, landscape changes in relation to the 1997–1998 El Niño event either occurred in the upstream reach of debris flow channels (e.g., Fig. 8e), or along the course of channels (Fig. 8b–d). It is also possible that high intensity rainfall during this period resulted in the formation of new channels. A possible candidate is seen on Fig. 8f that dissects an east-facing hillslope in a straight way, which is characteristic for a channel-forming debris flow event. In contrast, the Sechura desert did not experience gullying and substantial erosion despite the facts that (1) this region experiences maximum precipitation during El Niños, (2) this area is made up of a thick layer of unconsolidated sediment prone to erosion (Schneider et al. 2008) and that (3) this segment generally displays a high surface roughness (caused by e.g., the dune fields). We explain this lack of response compared to the uplands by the absence of a linked channel network. It is likely that the original Pleistocene topography of the desert, i.e., the presence of eolian dunes, precluded the initiation of a linked channel network. Second, the desert lies at sea level and thus offers a limited potential energy that appears insufficient for channels to initiate and propagate.

Conclusion

In this paper, we localize and identify landscape changes using SAR techniques in general and SAR intensity change and variance in particular. We show that with basic field calibration and data processing, it is possible to detect areas that possibly experienced focused surface change by mass wasting and gullying. This technique can be applied with good degree of confidence even for the situation where the frequency of SAR data registration is not optimum. Specifically, even for the case of the Piura drainage basin where the time difference between image acquisitions is approximately 4 years, the calculated pattern of mean intensity and variance difference yielded results that can be interpreted in terms of relationships between the channel network and surface erosion. Hence, SAR allows for assigning the locations in which the landscape has changed due to focused erosion, and where sediment has been delivered to the sediment routing system.

This study shows that the 1997–1998 El Niño resulted in surface erosion for locations that are coupled with the channel network. Similarly, it was argued by Schneider et al. (2008) that this particular El Niño period not only resulted in an efficient export of sediment, but that this climatic perturbation also promoted channelized processes

and downcutting. On the other hand, based on the results of the first step of our analyses, we considered the pattern of precipitation in relation to the Bolivian High to promote sediment production by weathering. As argued by von Blanckenburg (2005), weathering rates would decay if hillslopes would not become refreshed by erosion. Hence, an increase in sediment production rates preconditions that sediment is being removed efficiently. This was the case during the e.g., 1997–1998 El Niño period as shown by the measurements at the Piura gauging station and the results of the second step of our analyses. On the other hand, rivers in general, and the Piura River in particular, would not deliver sediment to the sink if no sediment would be available. This implies that in the absence of the Bolivian High as a weathering agent, the Piura River would become undersaturated during El Niño periods. It appears, therefore, that the situation of a twofold climate, as seen in the Piura region, provides the condition to maximize sediment flux. In conclusion, we support the Molnar et al. (2006) statement that the sediment routing system will be efficient mainly in the stage of maximum energy. But we see a need that the sediment is made available through weathering in a first stage. Hence, an efficient sediment routing system not only requires high energy discharge events, but also a 'low energy' seasonal climate to produce the sediment.

References

Albertz J (2007) Einführung in die Fernerkundung, Grundlagen der Interpretation von Luft- und Satellutenbildern, 3rd edn. Wissenschaftliche Buchgesellschaft, pp 264

Barry RG, Chorley RJ (1998) Atmosphere, weather and climate. Routledge, London, p 536

Birot P (1968) The cycle of erosion in different climates. B. T. Batsford Ltd, London, p 144

Bjerknes J (1969) Atmospheric teleconnections from the equatorial Pacific. Mon Weather Rev 97:163–172. doi:10.1175/1520-0493(1969)097<0163:ATFTEP>2.3.CO;2

Coates AG, Jackson JBC, Collins LS, Cronin TM, Dowsett HJ, Bybell LM et al (1992) Closure of the Isthmus of Panama: the nearshore marine record of Costa Rica and western Panama. Geol Soc Am Bull 104:814–828. doi:10.1130/0016-7606(1992)104<0814:COTIOP>2.3.CO;2

Cobbing EJ, Pitcher WS, Wilson JJ, Baldock JW, Taylor WP, McCourt WJ et al (1981) The Geology of the Western Cordillera of Northern Perú: London. Overseas Mem Inst Geol Sci 5:144

Crosetto M, Crippa B, Biescas E, Monserrat O, Agudo M, Fernandez P (2005) Land deformation measurement using SAR interferometry: state-of-the-art. Photogramm Fernerkundung Geoinf 6:497–510

Curry JA, Webster PJ (1999) Thermodynamics of atmospheres and oceans. Academic Press, London, p 471

Fruneau G, Achache J, Delacourt C (1996) Observation and modelling of the Saint-Etienne-De-Tinée landslide using SAR interferometry. Tectonophysics 265:181–190. doi:10.1016/S0040-1951(96)00047-9

Garreaud RD, Aceituno P (2001) Interannual rainfall variability over the South American Altiplano. J Clim 14:2779–2789. doi:10.1175/1520-0442(2001)014<2779:IRVOTS>2.0.CO;2

Goldberg RA, Tisnado M, Scofield RA (1987) Characteristics of extreme rainfall events in northwestern Peru during the 1982–1983 El Niño period. J Geophys Res 92:14225–14241. doi:10.1029/JC092iC13p14225

Grimm AM, Vera CS, Mechoso CR (2005) The South American monsoon system. In: Chang C-P, Wang B, Lau GNC (eds) The global monsoon system research and forecast. World Meteorology Organization TD-1266, Geneva, pp 219–238

Henderson F, Lewis A (eds) (1998) Principles and applications of imaging radar. Wiley, New York, p 866

Horel JD, Cornejo-Garrido AG (1986) Convection along the Coast of Northern Peru during 1983: spatial and temporal variation of clouds and rainfall. Am Meteorol Soc 114:2091–2105

Hovius N, Stark CP, Tutton MA, Abbott LD (1998) Landslide-driven drainage network evolution in a pre-steady-state mountain belt: Finisterre Mountains, Papua New Guinea. Geology 26:1071–1074. doi:10.1130/0091-7613(1998)026<1071:LDDNEI>2.3.CO;2

Huber M, Caballero R (2003) Eocene El Niño: evidence for robust tropical dynamics in the "Hothouse". Science 299:877–881. doi:10.1126/science.1078766

Jaillard E, Hérail G, Monfret T, Díaz-Martínez E, Baby P, Lavenu A, et al (2000) Tectonic evolution of the Andes of Ecuador, Peru, Bolivia and northernmost Chile. In: Cordani UJ, Milani EJ, Thomaz Filho A, Campos DA (eds) Tectonic evolution of South America: Rio de Janeiro. 31st International Geological Congress, pp 481–559

Kirchner JW, Finkel RC, Riebe CS, Granger DE, Clayton JL, King JG et al (2001) Mountain erosion over time10 y, 10 k.y., and 10 m.y. scales. Geology 29:591–594. doi:10.1130/0091-7613(2001)029<0591:MEOYKY>2.0.CO;2

Kober F, Ivy-Ochs S, Schlunegger F, Baur H, Kubik PW, Wieler R (2007) Denudation rates and a topography-driven rainfall threshold in northern Chile: multiple cosmogenic nuclide data and sediment yields budgets. Geomorphology 83:97–120. doi:10.1016/j.geomorph.2006.06.029

Lillesand T, Kiefer R (2003) Remote sensing and image interpretation, 5th edn. Wiley, New York, p 763

Molnar P, Anderson R, Kier SG, Rose J (2006) Relationships among probability distributions of stream discharges in floods, climate, bed load transport, and river incision. J Geophys Res 111:F02001. doi:10.1029/2005JF000310

Oliver C, Quegan S (2004) Understanding synthetic aperture radar images. SciTech Publishing Inc, Raleigh, p 479

Ormsby J, Blanchard B, Blanchard A (1985) Detection of lowland flooding using active microwave systems. Photogramm Eng Remote Sens 51:317–328

Philander SGH (1983) El Niño southern oscillation phenomena. Nature 302:295–301. doi:10.1038/302295a0

Pilger RH (1981) Plate reconstructions, aseismic ridges, and low-angle subduction beneath the Andes. Geol Soc Am Bull 92:448–456. doi:10.1130/0016-7606(1981)92<448:PRARAL>2.0.CO;2

Ramos VA, Aleman A (2000) Tectonic evolution of South America. In: Cordani UJ, Milani EJ, Thomaz Filho A, Campos DA (eds) Tectonic evolution of South America: Rio de Janeiro. 31st International Geological Congress, pp 635–685

Ravelo AC, Andreasen DH, Lyle M, Lyle AO, Wara MW (2004) Regional climate shifts caused by gradual global cooling in the Pliocene epoch. Nature 429:263–267. doi:10.1038/nature02567

Reiners PW, Ehlers TA, Mitchell SG, Montgomery DR (2003) Coupled spatial variations in precipitation and long-term erosion rates across the Washington Cascades. Nature 426:645–647. doi:10.1038/nature02111

Reynolds RW, Smith TM (1995) A high-resolution global sea surface temperature climatology. J Clim 8:1571–1583. doi:10.1175/1520-0442(1995)008<1571:AHRGSS>2.0.CO;2

Schneider H, Schwab M, Schlunegger F (2008) Channelized and hillslope sediment transport and the geomorphology of mountain belts. Int J Earth Sci 97:179–192. doi:10.1007/s00531-006-0164-9

Smith LC (2002) Emerging applications of interferometric synthetic aperture radar (InSAR) in geomorphology and hydrology. Ann Assoc Am Geogr 92:385–389. doi:10.1111/1467-8306.00295

Strasser M, Schlunegger F (2005) Erosional processes, topographic length-scales and geomorphic evolution in arid climatic environments: the 'Lluta collapse', northern Chile. Int J Earth Sci 94:433–446. doi:10.1007/s00531-005-0491-2

Toggweiler JR, Dixon K, Broecker WS (1991) The Peru upwelling and the ventilation of the South Pacific thermocline. J Geophys Res 96:20467–20497. doi:10.1029/91JC02063

Ulaby FT, Moore KM, Fung KM (1986) Microwave remote sensing, active and passive. vol 1–3, Norwood

von Blanckenburg F (2005) The control mechanisms of erosion and weathering at basin scale from cosmogenic nuclides in river sediment. Earth Planet Sci Lett 237:462–479. doi:10.1016/j.epsl.2005.06.030

Wara MW, Ravelo AC, Delaney ML (2005) Permanent El Niño-like conditions during the Pliocene Warm Period. Science 309:758–761. doi:10.1126/science.1112596

Wipf M, Zeilinger G, Seward D, Schlunegger F (2008) Focused subaerial erosion during ridge subduction: impact on the geomorphology in south-central Peru. Terra Nova 20:1–10

Woodman R (1998) El Fenomeno El Niño y el Clima en el Peru. In: El Perú en los Albores del Siglo XXI/2 (Ciclo de Conferencias 1997–1998). Ediciones del Congreso del Perú, Lima, Peru, pp 201–242

Zebker HP, Rosen A, Goldstein RM, Gabriel A, Werner CL (1994) On the derivation of coseismic displacement fields using differential radar interferometry: the Landers earthquake. J Geophys Res 99:19617–19634. doi:10.1029/94JB01179